

# **Large Eddy Simulations of Effect of Double-Ruler Electro-magnetic Field on Transient Flow during Continuous Casting**

R. Singh, B.G. Thomas and S.P. Vanka

Mechanical Science and Engineering Department,  
University of Illinois at Urbana-Champaign,  
Mechanical Engineering Building, 1206 W. Green St, Urbana, IL, 61801, USA

Phone: (217)333-6919

Email: rsingh28@illinois.edu, bgthomas@illinois.edu,  
spvanka@illinois.edu

## **Abstract**

Transient flow during nominally steady conditions is responsible for many intermittent defects during continuous casting of steel. The double-ruler electromagnetic field configuration, or “FC-Mold EMBR,” is popular in commercial slab casting as it provides independent control of the applied static field near the jet and free surface regions of the mold. In the present study, transient flow in a typical commercial caster is simulated without and with a double ruler magnetic field, with rulers of equal strengths. Large eddy simulations with the in-house code CU-FLOW resolve the important transient behaviour, using grids of over five-million cells with a fast parallel solver. Without a magnetic field, a double-roll pattern is observed, with transient unbalanced behavior, high surface velocities, ( $>\sim 0.5\text{m/s}$ ) surface vortex formation, and very large surface level fluctuations ( $\sim \pm 12\text{ mm}$ ). Applying the magnetic field suppresses the unbalanced behaviour, producing a more complex mold flow pattern, but with much lower surface velocities, ( $<\sim 0.1\text{m/s}$ ), and a flat surface level with small level fluctuations ( $<\pm 1\text{mm}$ ). Nail board measurements taken at this commercial

caster, without the field, matched reasonably well with the calculations, both quantitatively and qualitatively.

## **1. Introduction**

The quality of steel products is greatly affected by the stability of fluid flow near the top surface of the mold during the continuous casting process. Maintaining steady-state casting conditions is well known to produce the most stable flow and best quality. The steady flow pattern depends on the nozzle geometry, casting speed, mold width, mold thickness, argon gas injection, and submergence depth. In conventional slab casting, if the jet impinges first on the free surface, a “single-roll” flow pattern is generated. If the jet first impinges on the narrow face, and splits, flowing up towards the free surface, a “double-roll” flow pattern is generated. When the control parameters create conditions which fall on the borderline between single and double roll, then complex unstable flow conditions are likely. The highly-turbulent nature of flow in the mold causes transient behaviour even during statistically-steady state operation. Sudden increases in velocity, level fluctuations, vortex formation, and other intermittent flow events can lead to the entrainment of mold slag, the formation of surface defects, and other quality problems. One of the only process parameters that can respond to changes during steady turbulent flow is the application of electromagnetic forces.

In steel slab casting, both static and moving magnetic fields have been implemented. Statically-applied electro-magnetic-field (EMF) configurations include local (circular fields on each side of the SEN) [1-5], single-ruler (a rectangular field across the entire mold width) [5,6] and double-ruler [6-9] (two ruler-shaped fields, with one positioned across the mold near the meniscus and the other one aligned through or below the nozzle ports). When the EMF coil currents are adjusted to produce equal peak field strengths, this double-ruler configuration is commercially known as “Flow-Control-Mold” or “FC-Mold” ElectroMagnetic Braking or “EMBr”. The regions of strongest magnetic tend to deflect the

flowing steel, altering the time-averaged flow, which has been the subject of many previous modelling studies [1,3,4,6,10,11-13]. The effect on transient flow has received less study.

The flow of a conducting fluid such as steel through a magnetic field generates a force opposing the motion, and thus should be self-stabilizing. However, the magnetic field can change the flow stability in non-obvious ways [6]. Previous work has shown that conducting walls, such as the solid steel shell surrounding the liquid cavity in continuous casting, have a stabilizing effect on the flow. For example, Large Eddy Simulations (LES) and UDV measurements of mold flow in a scaled physical model with GaInSn, a low melting liquid metal alloy, were performed to study the effect of ruler Electromagnetic Braking (EMBr) on transient flow phenomena, with conducting (brass) versus insulated (plastic) side walls [12,13]. The application of a single-ruler EMBr over the nozzle with insulated walls made the mold flow unstable, with large scale wobbling of the jets. With insulating walls, the current loops returning through the molten steel induce forces which deflect the local current-carrying flow, carrying its accompanying flow destabilizing effects elsewhere in a chaotic-feedback manner. This behavior is suppressed with conducting side walls, such as the solidifying steel shell of a real caster. This is because the forces induced by current loops returning through the solid shell have no effect.

In the present study, we perform two large eddy simulations of the mold flow in a real commercial caster to investigate the effect of an applied double-ruler EMBr magnetic field configuration. The transient and time-averaged results of the two simulations performed with and without electromagnetics are compared, focussing on surface flow phenomena. Nail board measurements were also taken at the commercial caster, without any applied magnetic field, and are compared with the calculated results.

## 2 Computational Model Description

### 2.1 Governing Equations for LES of MHD Flow

In this study, we solve the unsteady three-dimensional continuity and momentum equation given by Equations 1 and 2 respectively.

$$\frac{\partial u_j}{\partial x_j} = 0 \quad (1)$$

$$\frac{\partial u_i}{\partial t} + \frac{\partial u_i u_j}{\partial x_j} = -\frac{1}{\rho} \frac{\partial p^*}{\partial x_i} + \frac{\partial}{\partial x_j} \left( (\nu + \nu_s) \left( \frac{\partial u_i}{\partial x_j} + \frac{\partial u_j}{\partial x_i} \right) \right) + \frac{1}{\rho} F_i \quad i = 1, 2, 3 \quad (2)$$

Here  $i, j$  imply tensor notation and repeated indices in a term indicate summation,  $u_i$  are the three velocity components,  $p^*$  is the pressure modified to include the filtered normal stresses ( $p^* = p + (1/3)\rho\tau_{kk}$ ), where  $p$  is the static pressure,  $\rho$  is the fluid density,  $\nu$  is the kinematic viscosity and  $F_i$  in Equation (1) represents the three Lorentz-force components. The effects of the flow phenomena too small to be captured by the grid spacing, and thus spatially filtered, are incorporated by an eddy viscosity  $\nu_s$  which is modeled with the Coherent-structure Smagorinsky Model (CSM) Sub-Grid Scale SGS model [17].

The molten steel flowing through the magnetic field generates an electric current  $\vec{J}$ , which flows through the entire domain to produce the Lorentz force  $\vec{F}$ , and is given by

$$\vec{J} = \sigma(\vec{E} + \vec{u} \times \vec{B}_0) = \sigma(-\vec{\nabla}\phi + \vec{u} \times \vec{B}_0) \quad (3)$$

This equation neglects the induced magnetic field, which is small compared to the applied magnetic field in this system [1,18]. The charge conservation condition,  $\nabla \cdot \vec{J} = 0$ , is then used to find the potential  $\phi$ .

$$\nabla \cdot (\sigma \nabla \phi) = \nabla \cdot (\sigma(\vec{u} \times \vec{B}_0)) \quad (4)$$

The Lorentz force  $\vec{F}$  is given by

$$\vec{F} = \vec{j} \times \vec{B}_0 \quad (5)$$

Here  $\sigma$  is electrical conductivity,  $\vec{E}$  is induced electric field,  $\phi$  is electric potential and  $\vec{B}_0$  is the applied magnetic field, which can be measured without flowing metal [8].

This set of coupled MHD equations (Eq. 1-5) is solved by the finite volume method and implemented on a graphics processing unit (GPU) for fast computation in the in-house code CUFLOW. The numerical details of solving these equations with CUFLOW have been discussed in previous works [19-22] and hence are only briefly described in Section 2.3.

## 2.2. Computational Domain

The complete geometry of the commercial caster, including the Upper Tundish Nozzle (UTN), the slide gate, the Submerged Entry Nozzle (SEN) with bifurcated round ports, and the mold, is given in Figure 1 and Table I. The computational domain for the present study included both the liquid region, shown in Figure 2, and a separate region consisting of the solidifying shell, which was initialized to move with the casting speed (Table I) in the casting direction. The slide gate, which moves perpendicular to the wide face (WF), is used as the flow control mechanism in the commercial caster. The position of the slide gate was 41.48 % open (36.5mm opening), which was calculated according to the liquid steel throughput rate, nozzle geometry, tundish height and argon gas injection rate using a model, based on Bernoulli's equation and empirical relations, developed by Liu and Thomas [23]. The shell thickness  $s$  at any given location below the meniscus was calculated from  $s = k\sqrt{t}$ , where  $t$  is the time (s) taken by the shell to travel the given distance and the constant  $k(= 2.75\text{mm}/\sqrt{s})$  was chosen to match the steady-state shell thickness profile (mm) based on break-out shell measurements by Iwasaki et. al. [24] for a similar caster.

### 2.3. Electromagnetic Field

A double-ruler EMBR configuration was applied with the maximum strength of the upper ruler and lower ruler fields occurring 60 mm and 560 mm below the free surface respectively. Figure 3 shows a contour plot of the applied magnetic field and Figure 4 shows its variation in the casting direction. The magnetic field applied here is adopted from a study by Idogawa et al. [8] on the effect of this EMBR configuration using experiments with a scaled mercury model, numerical simulations using a RANS model and experiments in a real caster. The field is assumed to be uniform in the width and thickness directions of the caster. Both rulers have only one non-zero magnetic field component, which acts in the Y-direction.

### 2.4. Mesh and Boundary Conditions

A Cartesian mesh was used in this study with 5.5 million finite volume cells. To generate the caster geometry, first a rectangular domain was meshed with 8.9 million cells. Then solid regions were blocked out. A uniform fixed-velocity boundary condition of 0.752m/s was applied at the inlet at the top of the UTN, based on the casting speed and the UTN inlet area. A no-slip boundary condition was applied on the free surface of the mold to approximately model the effects of the high viscosity slag on slowing down the steel/slag interface at the top surface [25]. A convective boundary condition was applied to the outlet of the caster for all three velocity components according to Equation 6.

$$\frac{\partial u_i}{\partial t} + U_{convective} \frac{\partial u_i}{\partial n} = 0 \quad i = 1,2,3 \quad (6)$$

Here  $U_{convective}$  is the average normal velocity across the outlet plane and  $n$  is the direction normal to the outlet plane. The solidifying shell was given fixed downward vertical velocity at the casting speed, which causes the liquid to leave the liquid domain to account for both mass transfer and momentum transfer from the fluid region to the solidifying shell. All other boundaries were treated as solid walls with the wall model of Werner and Wengle [26]. The

fluid flow equations were solved only in the fluid domain and the MHD equations were solved in the entire computational domain, including the solid shell. An insulated electrical boundary condition ( $\frac{\partial \phi}{\partial n} = 0$ ) was applied to the outermost boundary of the computational domain to simulate the non-conducting mold slag layer that surrounds the solid shell.

## **2.5. Numerical Method and Computational Cost**

CUFLOW solves the coupled MHD equations on a structured Cartesian grid using a NVIDIA Tesla C2075 Graphics Processing Unit (GPU). This code uses a fractional step method for the pressure-velocity coupling and the Adams Bashforth temporal scheme and second order finite volume method for discretizing the momentum equations. The pressure Poisson equation (PPE) and the electric Poisson equation (EPE) (Eq. 4) are solved using a geometric multigrid solver.

Simulations for both cases, No-EMBr and EMBr, were started from a zero initial velocity. The flowfields were allowed to develop for 10 seconds (200,000 time steps) and 20 seconds (400,000 time steps) for the No-EMBr and EMBr cases respectively before collecting the time-averages. Time-averages were stabilized for 5 seconds in both cases, and then turbulence statistics were collected for 20 seconds and 15 seconds for the No-EMBr and EMBr cases respectively. The computational expense of the EMBr case was nearly twice that of the No-EMBr case as it requires the solution of the electric Poisson equation (EPE). The 35 seconds of simulation without the magnetic field required a total of 15 days of calendar computation time, whereas the 40 seconds of simulation with the magnetic field took 34 days.

## **3. Transient Results**

### **3.1. Mold Flow**

The conditions for this caster (Table I) produce a typical “double-roll” flow pattern in the mold for both cases simulated, with strong flow across the top surface from the narrow face

towards the SEN, and a lower roll that penetrates deep into the strand. Figure 5a shows instantaneous contours of velocity magnitude in the mold region with no EMBr. Comparing these instantaneous snapshots clearly shows unbalanced flow, with transient asymmetries that alternate between the two halves of the mold. This unbalanced flow is not due to any geometric asymmetry. Displacement of the slide gate parallel to the wide faces results in a stationary unbalanced flow, but in this caster, the slide gate is displaced perpendicular to the narrow faces in a “90° orientation” [28-29]. This unbalanced flow is likely aggravated by the mountain-bottom (pointed-bottom) shape of this nozzle, which creates strong low-frequency fluctuations, relative to well-bottom nozzles [30]. The application of the EMBr field suppresses all of the scales of turbulence captured in this study, from small eddies (<1mm) to large side-to-side sloshing on the scale of the caster, as seen in Figure 5b. The jet velocity is dampened, which weakens the flow velocity in both the upper and lower rolls.

To quantify the unbalanced mold flow, Figure 6 compares the time history of a velocity component at two points (P1 and P3, shown in Figure 1) and their respective mirror images about the SEN centreline (P1\* and P3\*) for both the No-EMBr and EMBr cases. In the No-EMBr case, at both locations, very strong unbalanced flow behavior develops after ~15-20s. The transient unbalanced flow at the surface has temporal difference in surface velocities up to ~0.3m/s and at the jet region has maximum difference in jet velocities ~0.3m/s including reversal in direction. In addition, the unbalanced has strong spatial variations: sometimes strong surface flow is from right to left, (6a-top) and sometimes from left to right. This unbalanced flow can be detrimental because it tends to create more top surface fluctuations, vortex formation, upward flow impinging on the top surface, and slag crawling [31]. Unbalanced flow may also increase the penetration depth of inclusions and bubbles [32]. The application of the EMBr field damps this unbalanced behavior of mold flow as seen in Figure 6b at both locations.



### 3.2. Top Surface Behavior

Flow past bluff bodies results in vortex shedding which forms a Kármán vortex street. This phenomenon may occur near the SEN if an unbalanced flow between sides of the mold is observed in the top surface [33,34]. If accompanied by downward flow, these vortices at the surface can entrain a funnel of molten slag into the molten steel. However, the creation of these slag funnels does not necessarily result in entrainment of slag particles. If the height of the funnel is large enough to reach the jet region, the funnel is broken apart into droplets which are entrained into the jet, leading to slag entrapment in the product [34,35]. In a double-roll flow pattern, the flow down the SEN combined with vortices caused by any unbalanced surface flow, can lead to entrainment of liquid-slag funnels [36,37].

Figure 7 shows four instantaneous snapshots of the contours of velocity magnitude with vectors on the surface for both cases. The unbalanced surface flow from the right side in the No-EMBr case can be seen in the two snapshots,. This biased flow across the SEN leads to vortex shedding, with two strong vortices on the left of the SEN, as seen in the No-EMBr snapshot at 35 seconds. This pair of vortices persisted for ~3-4 s. The instantaneous plots for the EMBr case indicate no unbalanced flow. The surface velocities are smaller with EMBr (Note: Contour scale range and vector lengths are scaled five time larger with EMBr in Fig. 7) and show minimal fluctuations. The flow is mostly directed from the NF to the SEN, except close the SEN, where small recirculation regions form.

To visualize the paths of tracer particles in vortices and molten-slag funnels, instantaneous streamlines were plotted in Figure 8 at 35 s after the start of the simulation. With No-EMBr, these streamlines show how particles are indeed drawn across the surface from the right past the SEN into rotating vortices near the left of the SEN, and are sucked downward to become entrained into the swirling jet region. In contrast, with EMBr, the streamlines exhibit the simple recirculating flow behaviour typical of a double-roll flow

pattern. These results show that the No-EMBr case is more susceptible to the formation of the molten-slag funnels, and likely experiences more slag entrainment as a consequence.

Another mechanism for defect formation in the mold is due to the instability of the standing wave [31]. The standing wave is created by flow beneath the free surface and may become unstable if the local slope becomes too high [38]. In the present study, the surface level profile is approximated using Equation 7 [39] which estimates the liquid surface level by converting the pressure,  $p$ , at the top surface into potential energy.

$$Z_{sur} = \frac{p - p_{mean}}{\rho_{steel} g} \quad (7)$$

where the average pressure  $p_{mean}$  was calculated for the line along the top surface at the midplane between the wide faces,  $\rho_{steel}$  is steel density, and  $g$  is gravity  $9.81m/s^2$ . Figure 9 shows three typical “instantaneous” surface level profiles, averaged over 1 s time periods separated by 5 s intervals. The No-EMBr case has relatively large variations in surface level profile across the mold width, with the difference between the peak and the trough ranging from 10 mm to 21 mm. The highest levels are found near the NF and the SEN, with the level at the NF usually being higher. The high level at the NF is due to the high vertical velocity rising up the NF, whereas the elevated level at the SEN is due to the flow impinging on the SEN outer walls. The application of EMBr flattens the surface level almost completely with a maximum difference between the peak and trough only  $\sim 1.5$  mm. Another noticeable difference is that in the No-EMBr case the trough occurs midway between the NF and the SEN, whereas in the EMBr case, the trough occurs close to the SEN outer walls.

Excessive surface level fluctuation is another detrimental mechanism to steel quality, as it may expose the solidifying dendritic shell to the slag layer, causing entrainment leading to slivers just beneath the surface [40]. Level fluctuations in the present study were calculated

using Equation 7. Time histories of level fluctuations are shown in Figure 10 at two typical points, both 10mm below the free surface. The first is located close to midway point between the NF and the SEN (P1) and the second is located 50mm from the NF (P2). At both locations for the No-EMBr case there are appreciable turbulent small scales present and also large scale fluctuations with amplitudes of 5 to 10 mm. Both the small and large scale fluctuations are suppressed by the application of the magnetic field, resulting in stable surface behavior.

## **4. Time Averaged Results**

### **4.1. Nozzle Flow**

Figure 11 compares time-averaged velocity in the SEN region for both cases. The contour plots look symmetric for both cases indicating sufficient averaging time, which is due to the high velocities in this region. The mountain-bottom SEN produces thin and strong jets [30], which are observed in both cases. Flow inside the SEN ports is similar for both cases because the double-ruler EMBr configuration applies only a low magnetic field in the region around the SEN bottom. The jets exiting the ports have the same downward angle in both cases, although the jet with EMBr is deflected slightly upwards as it enters the mold. The applied magnetic field also reduces the velocities in the recirculation region above and below the jet.

To study the flow at the port exits, time-averaged velocity magnitude and TKE are shown along the vertical line on midplane between the wide faces, in Figure 12 and Figure 13 respectively. As expected, these variations are very similar for both the No-EMBr and the EMBr cases as the magnetic field has only a small effect in this region. The velocity magnitude is small at the top of the ports and remains low till midway between the top and bottom walls of the ports, after which it continuously rises reaching its maximum close to the

bottom of the port exits. The variation of TKE is more complicated. Slightly greater TKE is observed for the EMBR case everywhere along the port exit except close to the top. This is opposite to our understanding of the applied magnetic field suppressing turbulent fluctuations. However, this phenomenon can be explained by the fact that the flow inside the SEN is initially laminarized by the upper roller while entering the mold region and then becomes turbulent again as it reaches the nozzle bottom, where the magnetic field is weak.

#### **4.2. Mold Flow**

Figure 14 shows the streamlines and contours of time-averaged velocity magnitude in the mold region for the No-EMBR and the EMBR cases. The No-EMBR case exhibits a typical double-roll flow pattern, with the lower roll penetrating deep into the mold as mentioned earlier. The flowfield is almost symmetric after 25 seconds of averaging, with slight asymmetry in the lower roll indicating long-time transients. The flowfield is more complicated with the magnetic field. Velocities in the jet and the upper roll region are much slower. There are two small but strong recirculation zones just above and just below the jet which were observed previously [12]. Far below the lower recirculation zones, the flow eventually tends to be downwards across the entire section.

Large downward velocities below the jet region increase the penetration depth and the chances of bubbles and inclusions being captured into the solidified steel. Figures 15 and 16 show time-averaged vertical velocity profiles across the strand width at the midplane and across the strand thickness near the left NF ( $X=-0.8\text{m}$ ) respectively, at various vertical locations for both cases. The No-EMBR case has high downward near the NF, and returning flow up the center. The detrimental feature in the No-EMBR case is that the downward velocity near the NF remains high even at 1.6m from the free surface. The EMBR case has slower downward flow near the NF, which decreases with distance below the top surface.

The effect of the applied magnetic field on the turbulence can be understood by studying the time-averaged Reynolds stresses of the flow. Figure 17 shows contour plots of the normal components of the time-averaged Reynolds stresses and the Turbulent Kinetic Energy (TKE). Magnetic fields are known to suppress the turbulence in the flow of a conducting material [18] and this effect is seen here. The fluctuating components in the No-EMBr case extend along the jet, deep into the upper roll of the mold. In contrast, the EMBr field suppresses the turbulent fluctuations and restricts the Reynolds stresses to the jet region near the port exits, especially in the through-thickness direction of  $\overline{v'v'}$ . The  $\overline{u'u'}$  and the TKE values are relatively high at the surface for the No-EMBr case as compared to the EMBr case.

#### 4.3. Surface Flow

As discussed earlier, the surface flow is critical to the steel quality. Very high surface velocities may entrain slag due to shear-layer instability [31], whereas very low surface velocities make the meniscus prone to freezing. Thus, the ideal surface velocity should be within a safe operating window between the upper and lower thresholds to avoid both defect mechanisms. This ideal range for top surface velocity was reported as 0.26 m/s to 0.43 m/s [31], but the exact range should depend on the superheat, slag-layer properties, and other conditions. Figure 18a and 18b compare the time-averaged surface velocity profiles across the strand width and thickness respectively for both cases. Across the width, the No-EMBr case has a high surface velocity with the maximum ( $\sim 0.55$  m/s) found midway between the SEN and the NF. The surface velocity with EMBr is much smaller ( $< \sim 0.1$  m/s). The velocity profile across the thickness is nearly uniform. The EMBr case has a slight M-shaped profile, with maximum velocity close to the walls. This classic M-Shaped profile is observed in previous studies of MHD flow in high-aspect ratio channels through transverse magnetic fields [40].

Neither case has an optimal surface velocity profile within the accepted range. It is therefore recommended to tailor the magnetic field to achieve the desired surface velocity as the No-EMBr case has other problems, such as unbalanced flow. The surface velocity with EMBr could be increased by either moving the lower ruler upwards or decreasing the strength of the upper ruler.

## 5. Comparison with Nail Board Measurements

The Nail Board Measurement method is used extensively to study surface flow phenomena [41] and has been extended [42-44] to predict surface velocity quantitatively. This nail dipping test produces instantaneous snapshots of the surface flowfield. Figure 19 shows a schematic of the steps in the method. An array of steel nails is dipped into the molten steel for 3-5 seconds, and the flow around the nail is revealed by the shape of the solidified lumps. The kinetic energy of the molten steel is converted to potential energy, which raises the steel / slag interface where the flow impacts the nail, and slopes downward in the flow direction. Rietow and Thomas [43] performed CFD analyses of the nail dipping test and based on these calculations and validation measurements in a steel caster, Liu et al. [44] established a correlation between the surface velocity  $V_{lump}$  (m/s) and the lump height difference  $\Delta h_{lump}$  (mm) as

$$V_{lump} = 0.624 (d_{lump})^{-0.696} (\Delta h_{lump})^{0.567} \quad (8)$$

where,  $d_{lump}$  (mm) is the lump diameter.

The simulation with No EMBr was performed at the same operating condition as the nailboard measurements in the commercial caster, except that the 4.4% volume of argon gas that was injected into the SEN was not included in the model. Figure 20 shows photographs of one the nail boards. There were two rows of nails, spaced ~50mm apart, across the width

of the mold which are referred to as the row closer to the Outer Radius (OR) or Inner Radius (IR).

Figure 21 compares the calculated surface velocity magnitude across the mold width with the two rows of measurements based on Eq. 8. The measured velocities are generally higher near the NF, relative to the predictions, which show a maximum midway between the NF and SEN. This may be explained by the unbalanced mold flow for the No-EMBr case as discussed previously. The measurements may have been taken at an instant when there was dominant recirculation in this half of the mold. To check this, an instantaneous velocity magnitude profile is included in Figure 21 at time of higher unbalanced flow. The instantaneous profile maximum matches the measurements well, but its location is still midway between the SEN and NF. A likely explanation for this discrepancy is the neglect of argon gas effects on the calculated flow. The measured and calculated velocity vectors are compared in Figure 22. The directions generally correspond with a stable double-roll flow pattern. The observed degree of cross flow associated with velocity fluctuations also appears to match reasonably well.

The free surface level profile was also measured from the solidified lumps and compared with the model predictions in Figure 23. The heights of the two rows of solidified lumps were averaged to estimate surface level profile along the centerline. The measured and the predicted surface level match very closely if the measured profile is rotated. Pivoting about the center handle of the nail board to raise one end 10mm and lower the other end by 10mm could easily have been introduced while dipping the nail board manually into the mold. Even without considering this rotation, the trend of higher level on the narrow face, and lowest level midway between the SEN and NF is both predicted and measured, and agrees with previous work [45]. The variations of over 15mm in height are significant.

## 5. Summary and Conclusions

Large eddy simulations of a real caster at industrial operating conditions were conducted in the present study, both with and without an applied magnetic field with the double ruler or FC-Mold EMBr configuration.

Without EMBr, a classic double-roll flow pattern is observed with transient unbalanced flow. The upper recirculation regions have high velocities which cause large variations in the surface level profile, (up to ~22mm), large surface level fluctuations ( $\sim \pm 12\text{mm}$ ) and high surface velocities (up to  $\sim 0.6\text{m/s}$ ). The lower loops penetrate deep into the strand and also have unbalanced transient behavior.

With the double ruler magnetic field, the unbalanced flow behavior is damped, and the flow is much more stable. The jet is deflected downwards, which weakens the upper recirculation regions, resulting in a flatter surface level profile (up to  $\sim 1.5\text{mm}$ ), with extremely small level fluctuations ( $< \pm 1\text{mm}$ ) and lower surface velocities ( $< 0.1\text{m/s}$ ).

The magnetic field makes the flow more stable and lowers surface velocity to prevent entrainment. However, to lessen meniscus freezing problems, it might be beneficial to increase the surface flow by moving the lower ruler upward to deflect the jet upward or by reducing the magnetic field strength of the upper ruler.

The lower rolls exhibit small recirculation regions below the jet, and the flow below this region has low velocities which are mostly aligned in the casting direction. These low velocities below the jet region are beneficial by reducing the penetration depth and lower the chances of inclusions and bubbles being entrapped in the solidifying front deep in the caster.

The calculated surface velocities for the No-EMBr case were compared with nail board measurements taken at the commercial continuous caster. It is difficult to establish a fair



comparison as the measurements only provide an instantaneous snapshot of the highly transient surface flow, and the effect of argon gas was ignored in the model. However, the measured surface flow directions, velocity profile, and the free surface level profile all agree reasonably well with the computations.

## **7. Acknowledgments**

This work was supported by the National Science Foundation Grant CMMI 11-30882 and the Continuous Casting Consortium at the University of Illinois at Urbana-Champaign. The authors are also grateful to Mr. Jonathan Powers and Mr. Thomas Henry for making the Severstal casting facility at Dearborn, MI, USA, available for the experiments and for their help during the nail board measurements.

## **6. References**

1. K. Cukierski and B.G. Thomas., “Flow control with local electromagnetic braking in continuous casting of steel slabs.”, *Metallurgical and Materials Transactions B*, 2008, vol. 39, pp. 94-107.
2. D. Kim, W. Kim, and K. Cho., “Numerical simulation of the coupled turbulent flow and macroscopic solidification in continuous casting with electromagnetic brake.”, *ISIJ International*, 2000, vol. 40, pp. 670-676.
3. K. Takatani, K. Nakai, N. Kasai, T. Watanabe, and H. Nakajima., “Analysis of heat transfer and fluid flow in the continuous casting mold with electromagnetic brake.”, *ISIJ International*, 1989, vol. 29, pp. 1063-1068.
4. M.Y. Ha, H.G. Lee, and S.H. Seong., “Numerical simulation of three-dimensional flow, heat transfer, and solidification of steel in continuous casting mold with electromagnetic brake.”, *Journal of Materials Processing Technology*, 2003, vol. 133, pp. 322-339.

5. H. Harada, T. Toh, T. Ishii, K. Kaneko, and E. Takeuchi., “Effect of magnetic field conditions on the electromagnetic braking efficiency.”, *ISIJ International*, 2001, vol. 41, pp. 1236-1244.
6. R. Chaudhary, B. G. Thomas, and S. P. Vanka., “Effect of electromagnetic ruler braking (EMBr) on transient turbulent flow in continuous slab casting using large eddy simulations.”, *Metallurgical and Materials Transactions B*, 2012, vol. 43, pp. 532-553.
7. B. Li, T. Okane, and T. Umeda., “Modeling of molten metal flow in a continuous casting process considering the effects of argon gas injection and static magnetic-field application.”, *Metallurgical and Materials Transactions B*, 2000, vol. 31, pp. 1491-1503.
8. A. Idogawa, M. Sugizawa, S. Takeuchi, K. Sorimachi, and T. Fujii., “Control of molten steel flow in continuous casting mold by two static magnetic fields imposed on whole width.”, *Materials Science and Engineering: A*, 1993, vol. 173, pp. 293-297.
9. Y. Miki and S. Takeuchi., “Internal defects of continuous casting slabs caused by asymmetric unbalanced steel flow in mold.”, *ISIJ International*, 43 (10): 1548–1555, 2003.
10. T. Ishii, S.S. Sazhin, and M. Makhlof., “Numerical prediction of magnetohydrodynamic flow in continuous casting process.”, *Ironmaking & Steelmaking*, 1996, vol. 23, pp. 267-272.
11. Y. Hwang, P. Cha, Ho-Seok Nam, Ki-Hyeon Moon, and Jong-Kyu Yoon., “Numerical analysis of the influences of operational parameters on the fluid flow and meniscus shape in slab caster with EMBr.”, *ISIJ International*, 1997, vol. 37, pp. 659-667.
12. R. Singh, B.G. Thomas and S.P. Vanka, “Effects of a magnetic field on turbulent flow in the mold region of a steel caster”, *Metallurgical and Materials Transactions B*, pp.1-21, May 2013.

13. X. Miao, K. Timmel, D. Lucas, S. Ren, Z. Eckert, and G. Gerbeth., “Effect of an electromagnetic brake on the turbulent melt flow in a continuous-casting mold.”, *Metallurgical and Materials Transactions B*, 2012, vol. 43, pp. 954-972.
14. B. Li, T. Okane, , and T. Umeda, “Modeling of biased flow phenomena associated with the effects of static magnetic-field application and argon gas injection in slab continuous casting of steel,” *Metallurgical and Materials Transactions B*, vol. 32, no. 6, pp. 1053–1066, 2001.
15. Y. Miki and S. Takeuchi., “Internal defects of continuous casting slabs caused by asymmetric unbalanced steel flow in mold.”, *ISIJ International*, 43 (10): 1548–1555, 2003.
16. F. Nicoud and F. Ducros, “Subgrid-scale stress modelling based on the square of the velocity gradient tensor”, *Flow, Turbulence and Combustion*, 1999, vol. 62, pp. 183-200.
17. H. Kobayashi, “Large eddy simulation of magnetohydrodynamic turbulent channel flows with local subgrid-scale model based on coherent structures”, *Physics of Fluids*, 2006, vol. 18, pp. 045107.
18. R. Moreau., *Magnetohydrodynamics*, Kluwer Academic Pub. Co., Norwell, MA, 1990, pp. 110-64.
19. R. Chaudhary, S. P. Vanka, and B. G. Thomas, “Direct numerical simulations of magnetic field effects on turbulent flow in a square duct”, *Physics of Fluids*, 2010, vol. 22, pp. 075102-15.
20. R. Chaudhary, A.F. Shinn, S.P. Vanka, and B.G. Thomas, “Direct numerical simulations of transverse and spanwise magnetic field effects on turbulent flow in a 2:1 aspect ratio rectangular duct”, *Computers & Fluids*, 2011, vol. 51, pp. 100-114.

21. A.F. Shinn and S.P. Vanka, “Large eddy simulations of film-cooling flows with a micro-ramp vortex generator”, *Journal of Turbomachinery*, 2013, vol. 135, pp. 011004-16.
22. A.F. Shinn, “Large eddy simulations of turbulent flows on graphics processing units: application to film-cooling flows”, PhD Thesis, University of Illinois at Urbana-Champaign, 2011.
23. R. Liu and B.G. Thomas, “Transient turbulent flow simulation with water model validation and application to slide gate dithering.”, AISTech 2012 Steelmaking Conference Proc., Atlanta, GA, May 7-10, 2012.
24. J. Iwasaki and B.G. Thomas., “Thermal-mechanical model calibration with breakout shell measurements in continuous steel slab casting”, pp. 355–362. John Wiley & Sons, Inc., 2012. ISBN 9781118357002.
25. R. Chaudhary, B.T. Rietow, and B.G. Thomas., “Differences between physical water models and steel continuous casters: A theoretical evaluation.”, Inclusions in Clean Steel, Mater. Sci. Technol., AIST/TMS, Pittsburgh, PA, 2009, pp. 1090-1101.
26. H. Werner and H. Wengle., “Large-eddy simulation of turbulent flow over and around a cube in a plate channel.”, In *8th Symposium on Turbulent Shear Flows*, pages 155–168, 1991.
27. B.G. Thomas, “The making, shaping and treating of steel: Chap. 14: Fluid flow in the mold.”, 11th ed., Casting Volume, A.W. Cramb, ed., The AISE Steel Foundation, Warrendale, PA, 2003.
28. H. Bai and B. G. Thomas, “Turbulent flow of liquid steel and argon bubbles in slide-gate tundish nozzles: Part I. model development and validation,” *Metallurgical and Materials Transactions B*, vol. 32, no. 2, pp. 253–267, 2001.

29. H. Bai and B. G. Thomas, "Turbulent flow of liquid steel and argon bubbles in slide-gate tundish nozzles: Part II. Effect of operation conditions and nozzles design," *Metallurgical and Materials Transactions B*, vol. 32, no. 2, pp. 269–284, 2001.
30. R. Chaudhary, G.G. Lee, B.G. Thomas and S-H Kim, "Transient mold fluid flow with well- and mountain-bottom nozzles in continuous casting of steel", *Metallurgical and Materials Transactions B*, vol. 39, no. 6, pp. 870–884, 2008.
31. L. C. Hibbeler and B.G. Thomas, "Mold slag entrainment mechanisms in continuous casting molds", AISTech 2013 Steelmaking Conference Proc., Pittsburgh, PA, May 6-9, 2013.
32. Y. Miki and S. Takeuchi., "Internal defects of continuous casting slabs caused by asymmetric unbalanced steel flow in mold.", *ISIJ International*, 43 (10): 1548–1555, 2003.
33. D. Gupta and A. K. Lahiri, "Water-modeling study of the surface disturbances in continuous slab caster," *Metallurgical and Materials Transactions B*, vol. 25, no. 2, pp. 227–233, 1994.
34. S.-M. Cho, G.-G. Lee, S.-H. Kim, R. Chaudhary, O.-D. Kwon, and B. G. Thomas, "Effect of stopper-rod misalignment on asymmetric flow and vortex formation in steel slab casting," in Jim Evans Honorary Symposium, in Proceedings of The Minerals, Metals, and Materials Society 139th Annual Meeting, pp. 71–77, The Minerals, Metals, and Materials Society, 2010.
35. Q. He, "Observations of vortex formation in the mould of a continuous slab caster," *ISIJ International*, vol. 33, no. 2, pp. 343–345, 1993.
36. M. Gebhard, Q. He, and J. Herbertson, "Vortexing phenomena in continuous slab casting moulds," in 76th Steelmaking Conference Proceedings, pp. 441–446, The Iron and Steel Society, 1993.

37. J. W. Rottman, "Steep standing waves at a fluid interface," *Journal of Fluid Mechanics*, vol. 124, pp. 283–306, 1982.
38. R. Chaudhary, B.T. Rietow, and B.G. Thomas., "Differences between physical water models and steel continuous casters: A theoretical evaluation.", Inclusions in Clean Steel, Mater. Sci. Technol., AIST/TMS, Pittsburgh, PA, 2009, pp. 1090-1101.
39. C. Ojeda, B. G. Thomas, J. Barco, and J. Arana, "Model of thermal-fluid flow in the meniscus region during an oscillation cycle," in Proceedings of AISTech, vol. 2, pp. 269–283, The Association for Iron and Steel Technology, 2007.
40. J.C.R. Hunt, "Magnetohydrodynamic flow in rectangular ducts", *Journal of Fluid Mechanics*, vol. 21, part 4, pp. 577-590, 1965.
41. P.H. Dauby, W.H. Emling, and R. Sobolewski, "Lubrication in the mold: A multiple variable system." *Ironmaker and Steelmaker*, 1986. 13 (Feb): p. 28-36.
42. R. McDavid and B.G. Thomas, "Flow and thermal behavior of the top-surface flux powder layers in continuous casting molds", *Metall. Trans. B*, 1996. 27B (4): p. 672-685.
43. B. Rietow and B.G. Thomas, "Using nail board experiments to quantify surface velocity in the CC mold.", AISTech 2008 Steelmaking Conference Proc., Pittsburgh, PA, May 5-8, 2008.
44. R. Liu, J. Sengupta, D. Crosbie, S. Chung, M. Trinh and B.G. Thomas, "Measurement of molten steel surface velocity with SVC and nail dipping during continuous casting process.", *The Minerals, Metals & Materials Society*, 2011.
45. Q. Yuan, B.G. Thomas, and S.P. Vanka., "Study of transient flow and particle transport in continuous steel caster molds: PartI- Fluid flow.", *Metallurgical and Materials Transactions B*, 2004, vol. 35, pp. 685-702.

Table I- Process Parameters

	Real Caster
Mold width (L)	1706.0 mm
Mold thickness	203.2 mm
Nozzle port diameter	75.0 mm
Nozzle bore diameter (d) ( <i>inner</i>   <i>outer</i> )	70 mm   130 mm
Nozzle port angle	25.0 deg
Slide gate orientation [28-29]	90.0 deg
Slide gate opening fraction ( $f_A$ )	41.48%
SEN submergence depth (liquid surface to top of port)	220 mm
Total volume flow rate	8.1 L/s
Mass flow rate	3.4 tonne/min
Bulk velocity at UTN inlet	0.752 m/s
Bulk velocity at SEN cross section (U)	2.1 m/s
Casting speed	1.4 m/min
Argon gas injection (volume fraction)	4.37% (ignored)
Thickness of shell (uniform around perimeter)	$s(mm) = 2.75\sqrt{t(s)}$
Viscosity (steel)	$0.86 \times 10^{-6} m^2/s$
Fluid density (steel)	$7000 Kg/m^3$
Conductivity of liquid ( $\sigma_{liquid}$ )	$0.714 \times 10^6 1/\Omega m$
Conductivity of walls ( $\sigma_{wall}$ )	$0.787 \times 10^6 1/\Omega m$
Reynolds number, ( $Re = Ud_{inner}/\nu$ , based on nozzle diameter)	171,000
Reynolds number, ( $Re = UL/\nu$ , based on mold width)	41,66,000
Hartmann number ( $Ha = BL\sqrt{\sigma/\rho\nu}$ , based on mold width)	5,202
Froude number ( $Fr = U/\sqrt{gL}$ ), based on mold width)	0.513
Stuart number ( $N = B_0^2 L \sigma / \rho U$ ), based on mold width)	6.5
Cases	1. No-EMBr 2. With EMBr

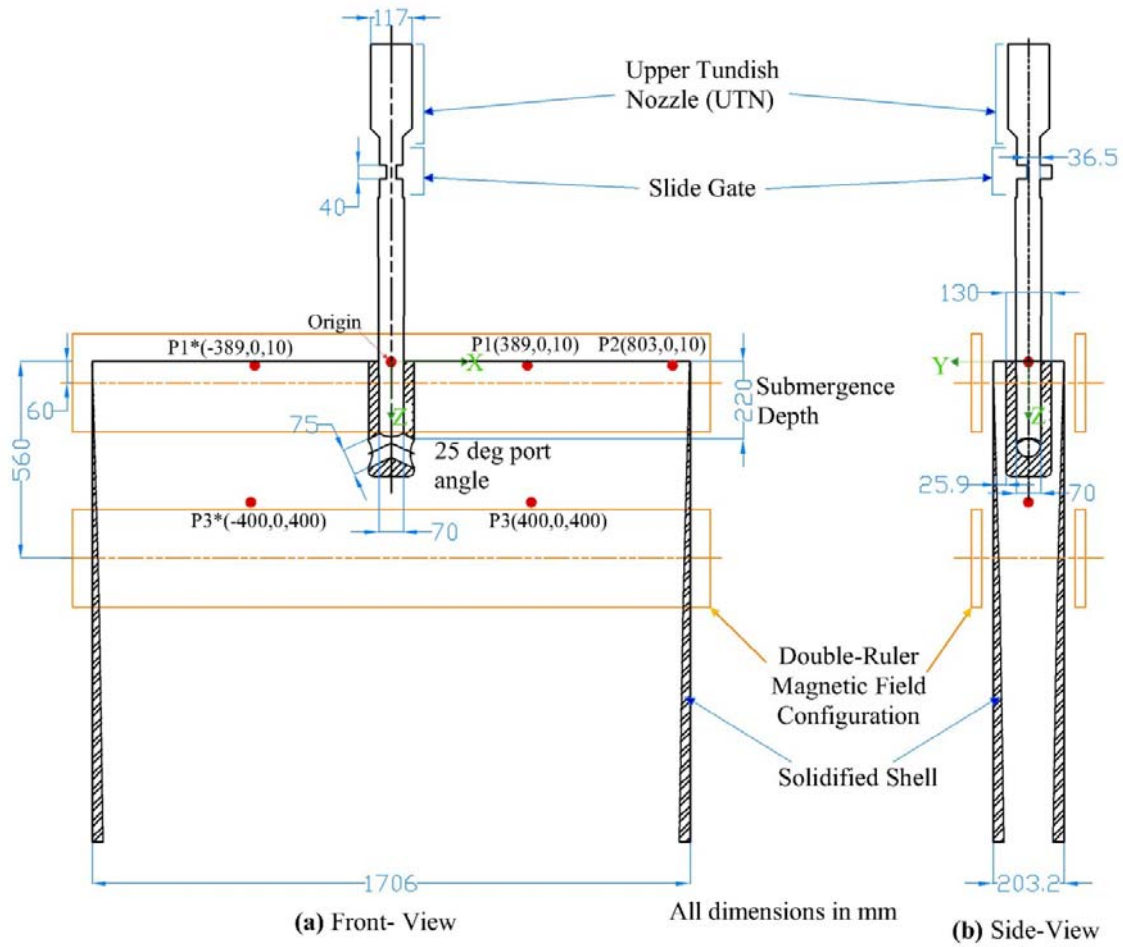


Figure 1- Geometry of the commercial caster with rectangles showing the location of the two rulers of the Double-Ruler EMBR



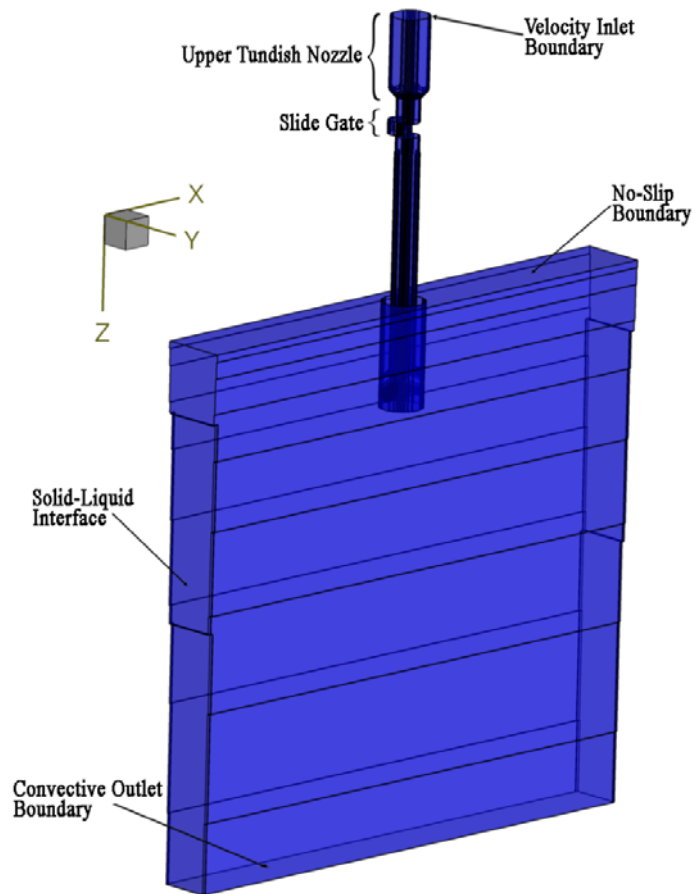


Figure 2- Isometric view of the computational domain (fluid flow region) with boundary conditions

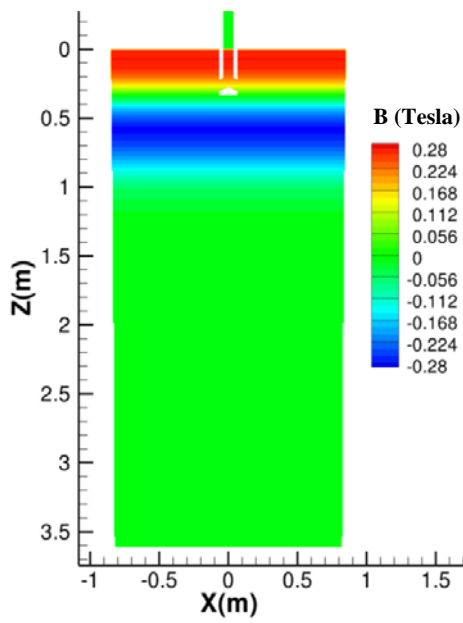


Figure 3- Contour plot of the applied magnetic field

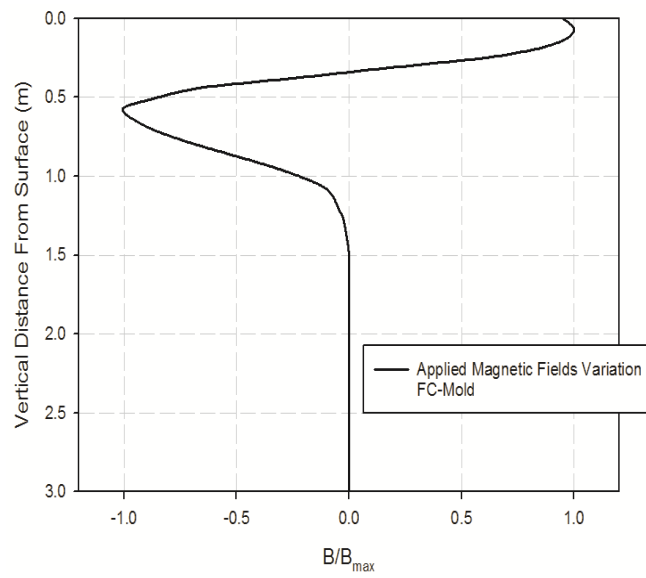


Figure 4- Variation of applied magnetic field in the casting direction ( $Z$ ) with  $B_{\max}=0.28$  Tesla in the EMBr case

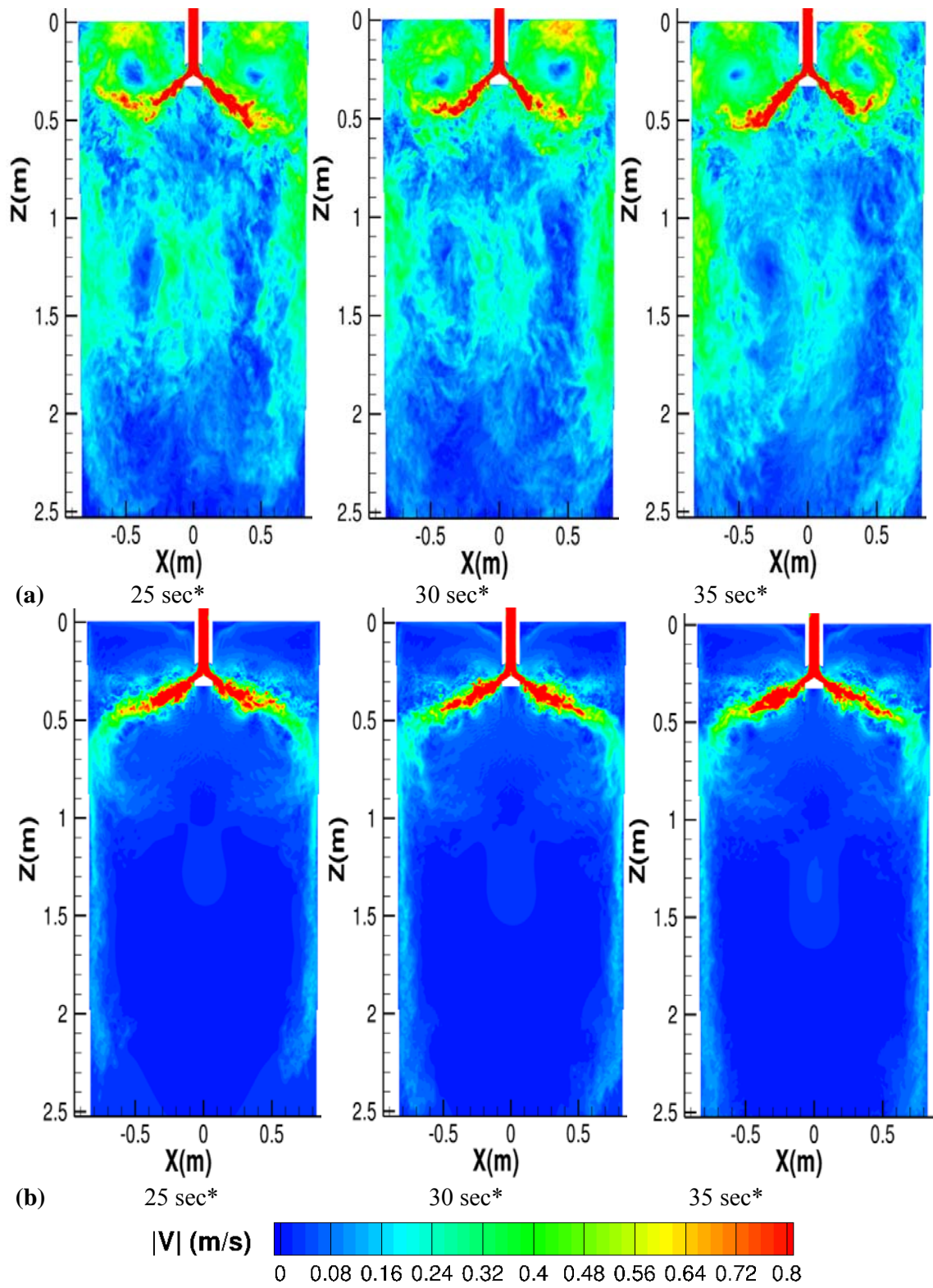
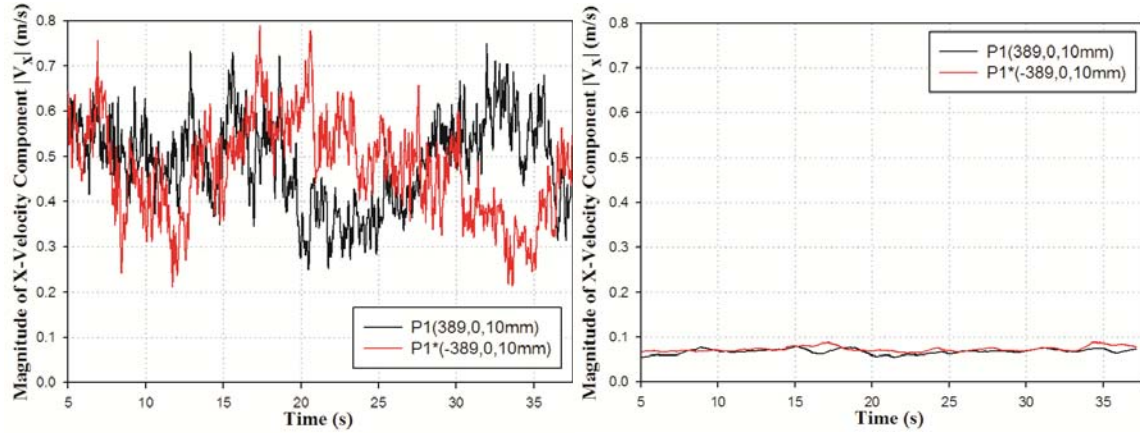
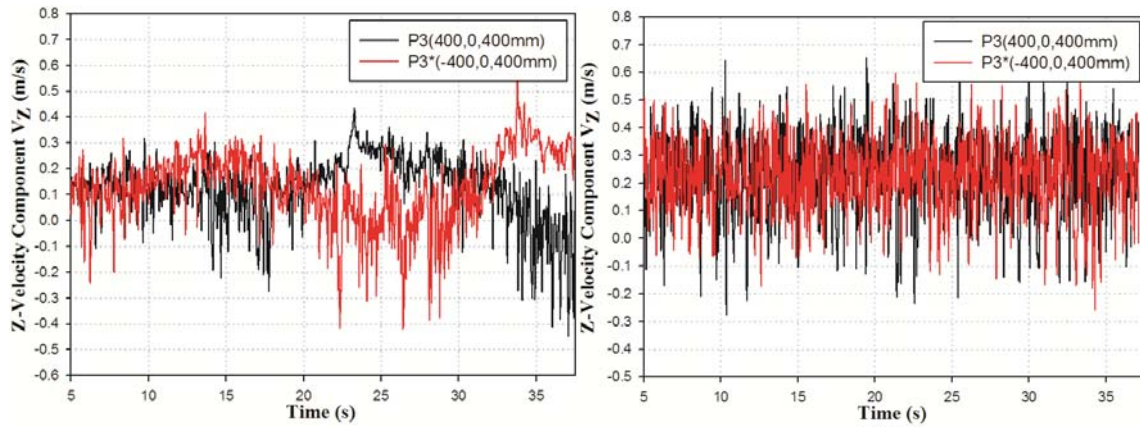


Figure 5- Contour plots of instantaneous velocity magnitude for (a) No-EMBr case and (b) EMBr case (\*Time from start of simulation)



Point P1 and P1\* are at the top surface close to midway between the SEN and the NF on each side of the mold



Point P3 and P3\* are in the jet region on each side of the mold  
 (a) No-EMBr (b) EMBr

Figure 6 Time history of velocity components showing unbalanced flow at mirror-imaged locations in the SEN centerline (P1 near surface and P3 in jet shown in Figure 1) (a) No-EMBr and (b) with EMBr

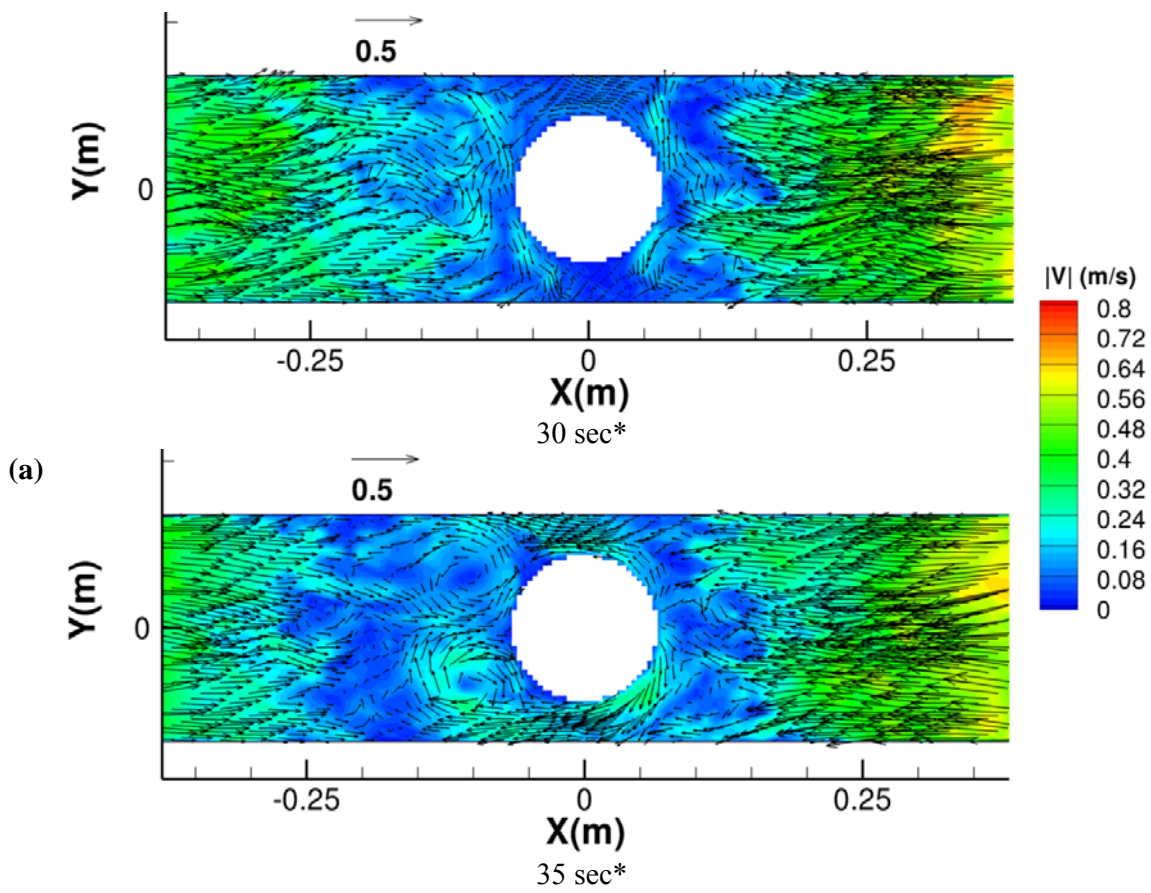


Figure 7- Contd.

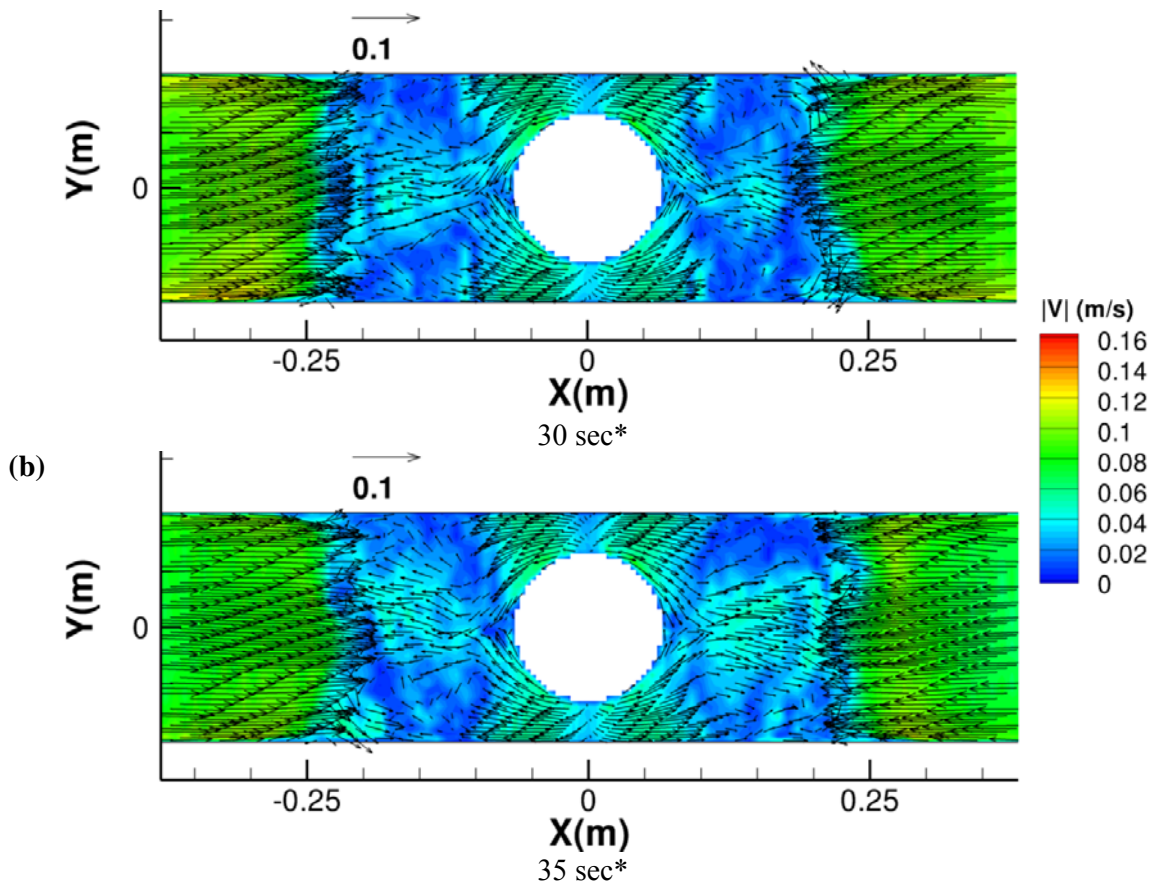


Figure 7- Contours of velocity magnitude with vectors, of  $V_x$  and  $V_y$ , 10mm from the top surface for (a) No-EMBr case and (b) EMBr case (\*Time from start of the simulation, 90% of vectors skipped for clarity)



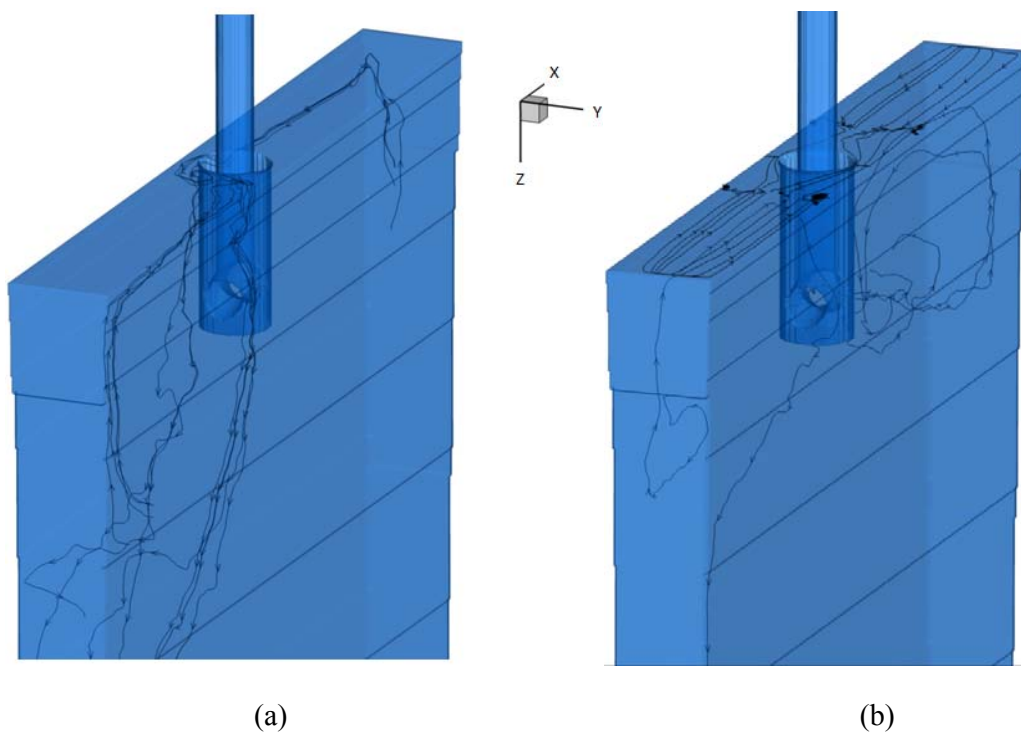


Figure 8- Streamlines of velocity for the (a) No-EMBr case and (b) EMBr case

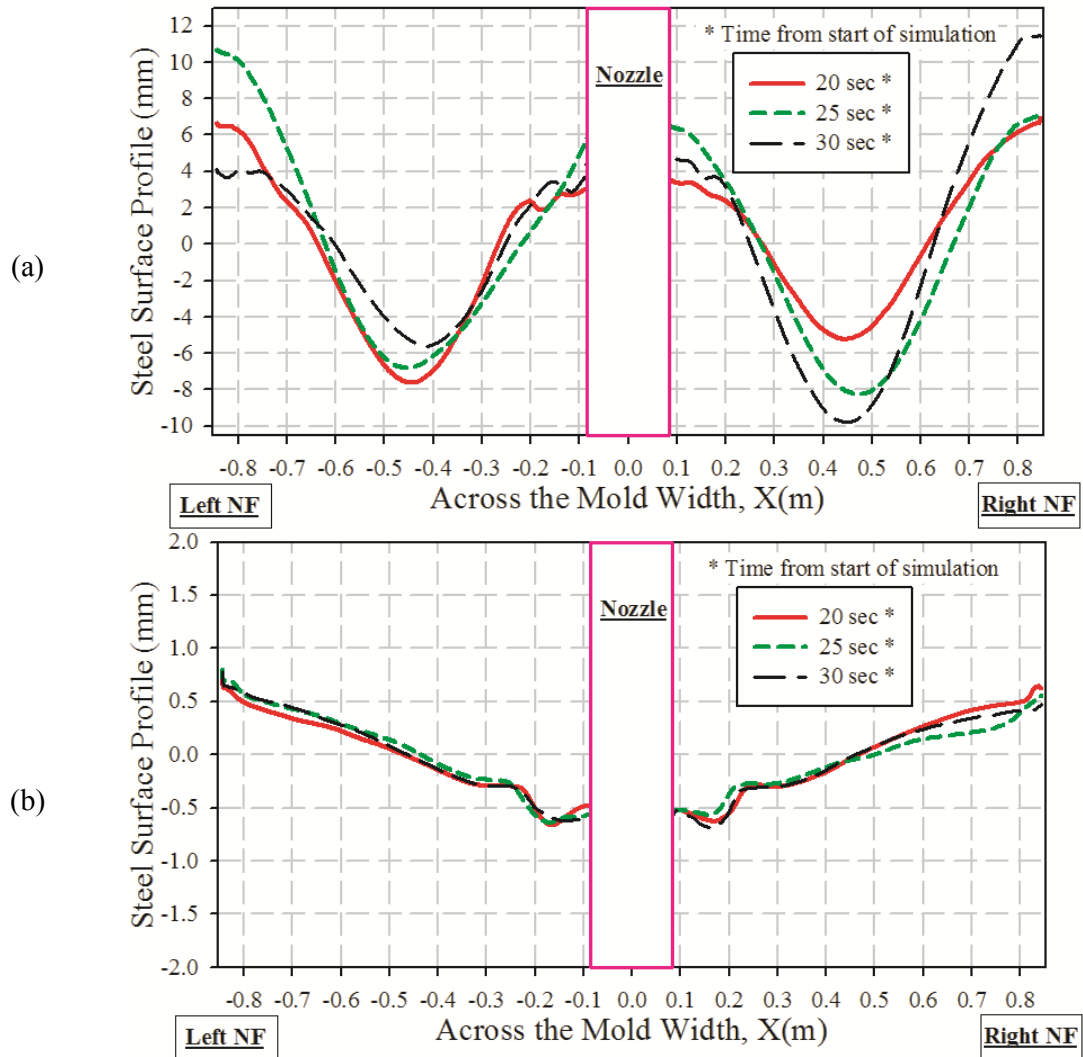


Figure 9- Surface level profiles at three instances for (a)No-EMBr case and (b) EMBr case



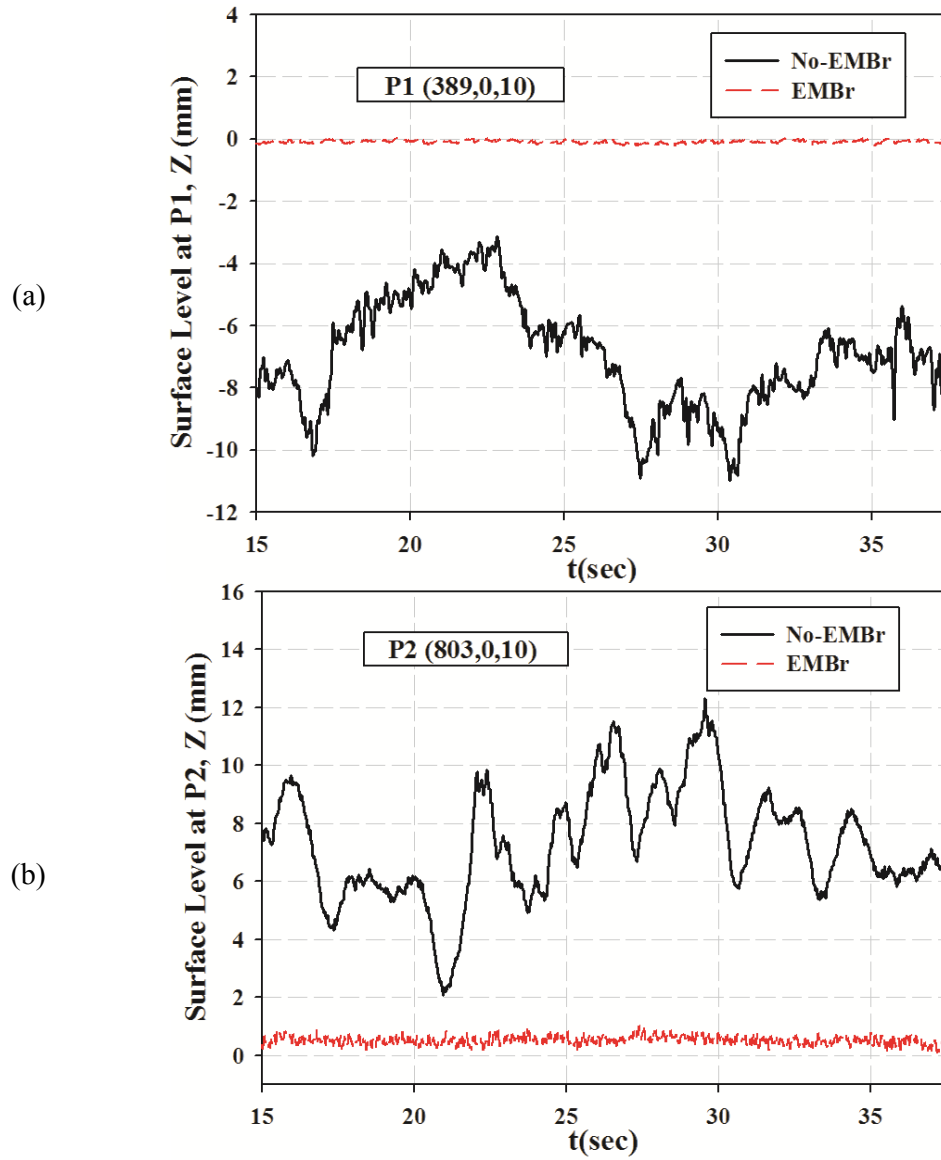


Figure 10- Time history of surface level fluctuations at points close to (a) midway between the narrow face and SEN, P1(389mm,0,10mm) (b) narrow face, P2(803mm,0,10mm)

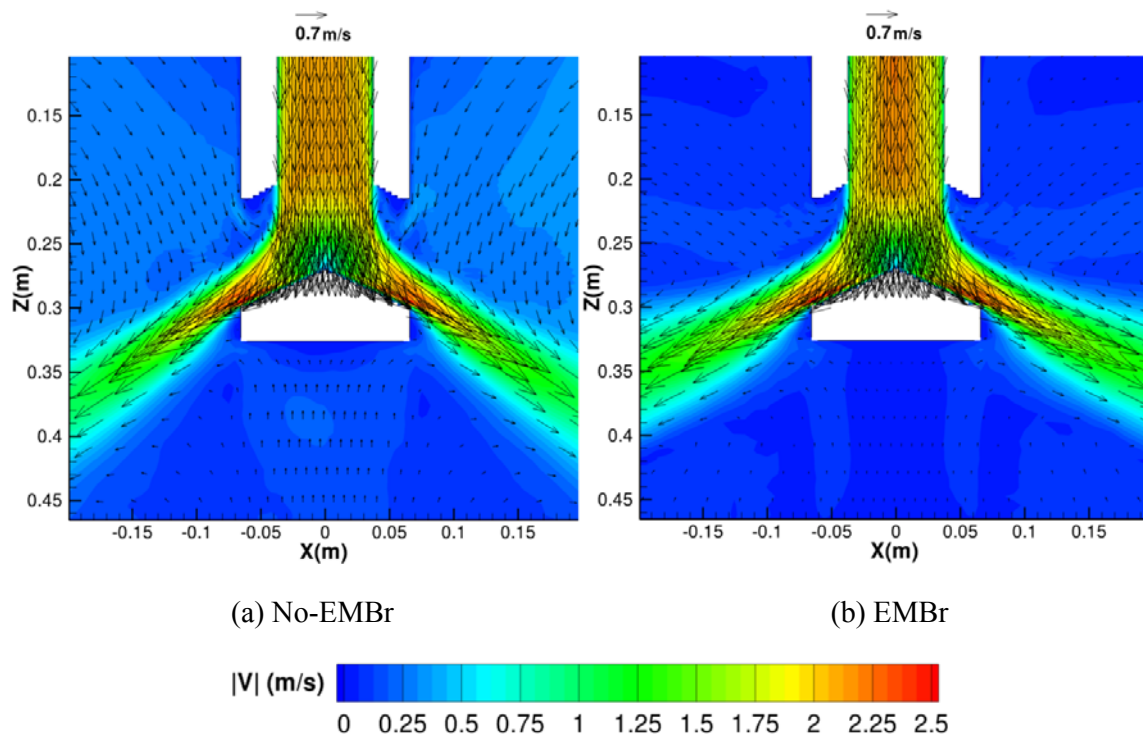


Figure 11- Contour plots of time-averaged velocity magnitude with vectors of  $V_z$  and  $V_x$  in the SEN region for (a) No-EMBr case and (b) EMBR case

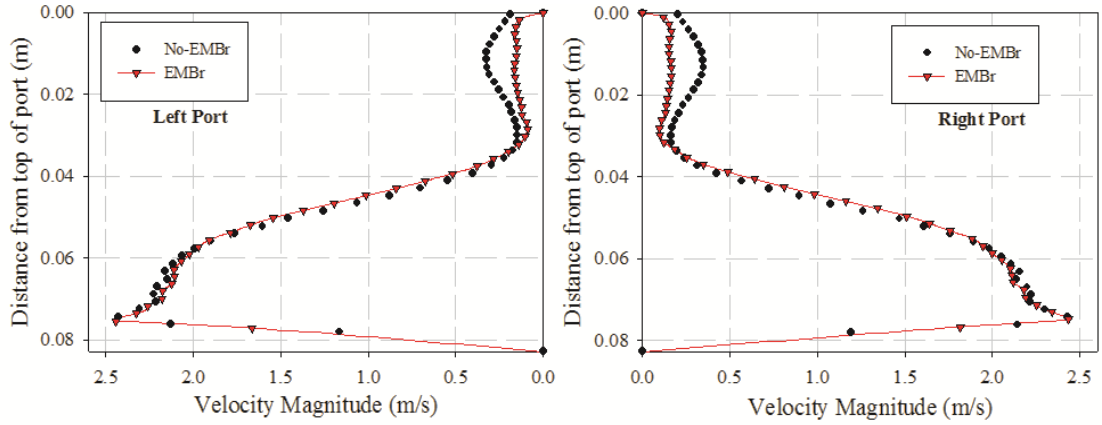


Figure 12- Variation of time-averaged velocity magnitude along a vertical line, on midplane between wide faces, at the port exits

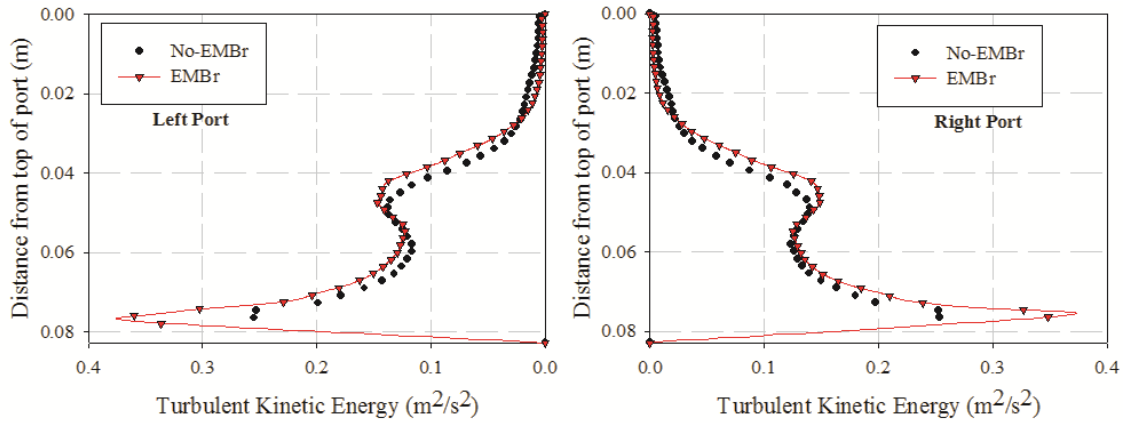


Figure 13- Variation of TKE along a vertical line, on midplane between wide faces, at the port exits

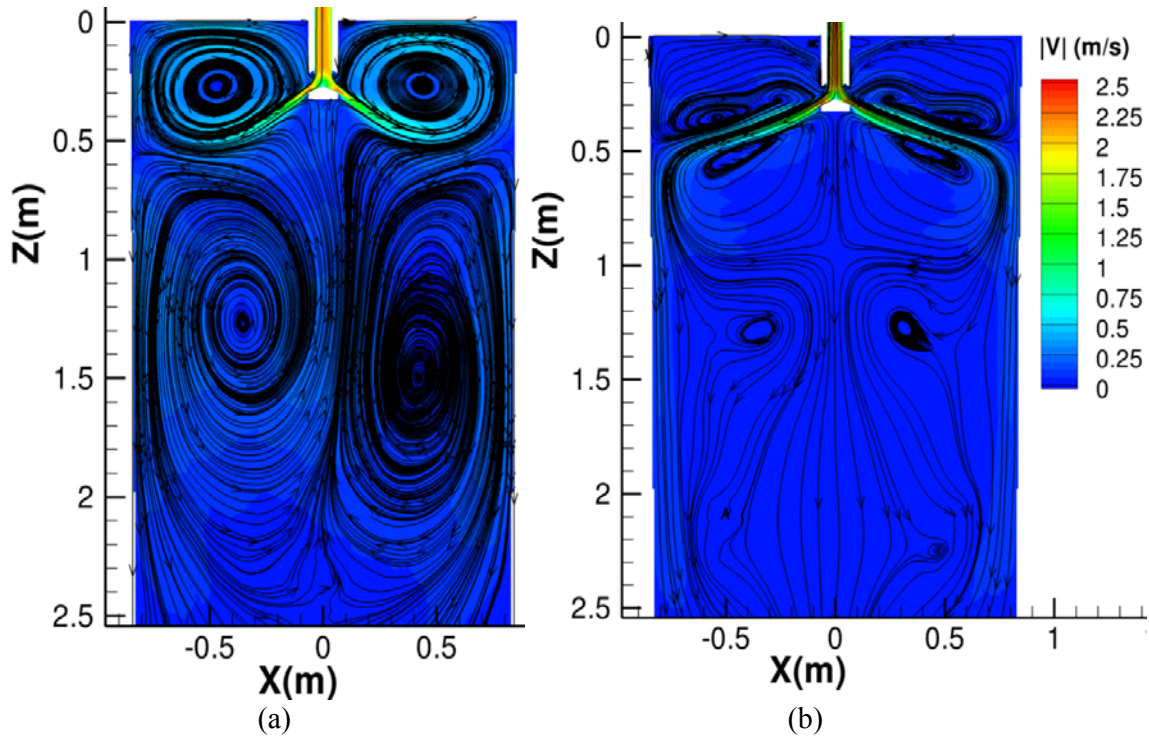


Figure 14- Contour plot of time-averaged velocity magnitude in the mold region with streamlines (a) No-EMBr (b) EMBr

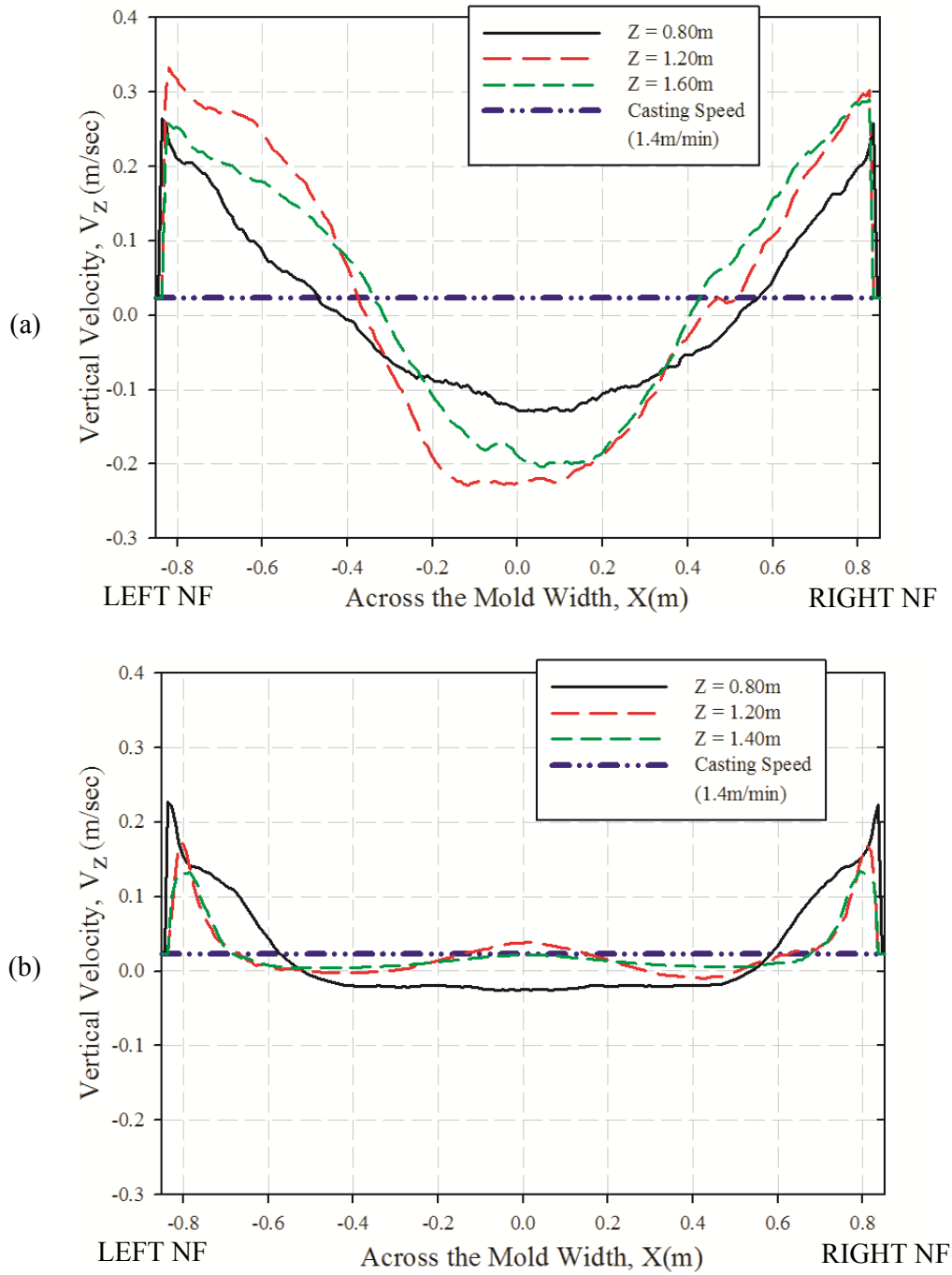


Figure 15- Time-averaged vertical velocity ( $V_z$ ) at four vertical locations in the midplane parallel to the mold wide face ( $Y=0\text{m}$ ) plotted across the mold width for (a) No-EMBr case and (b) EMBr case

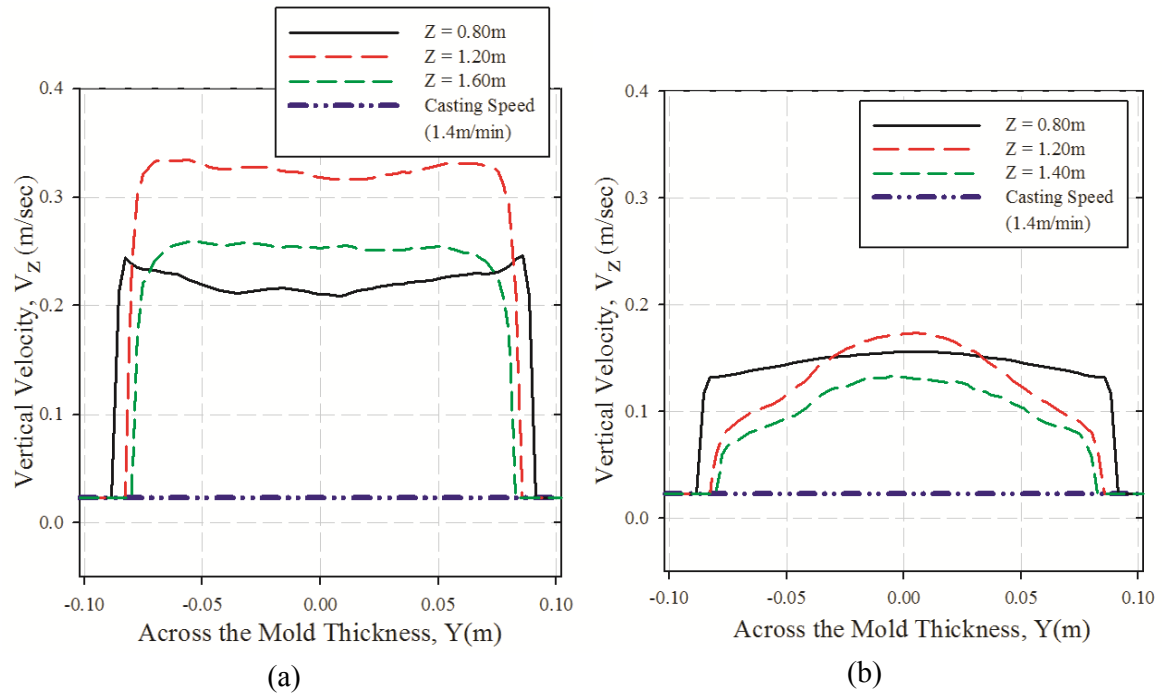


Figure 16- Time-averaged vertical velocity ( $V_z$ ) at four vertical locations in the midplane parallel to the mold wide face plotted across the mold thickness at  $X=-0.8$ m for (a) No-EMBr case and (b) EMBr case

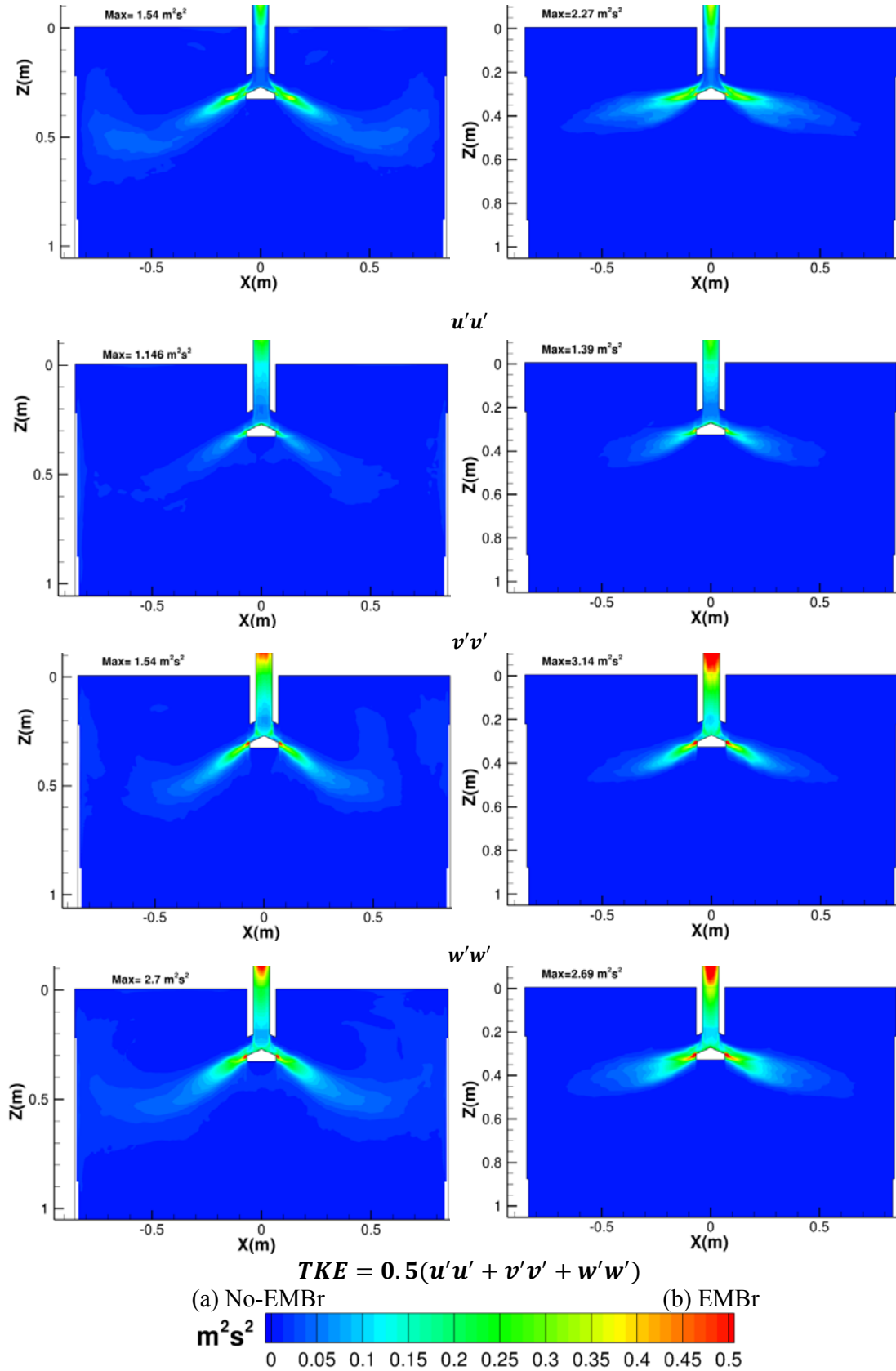


Figure 17- Contour plots of normal components of Reynolds stresses and Turbulent Kinetic Energy (TKE) in the mold region for (a)No-EMBr case and (b)EMBr case

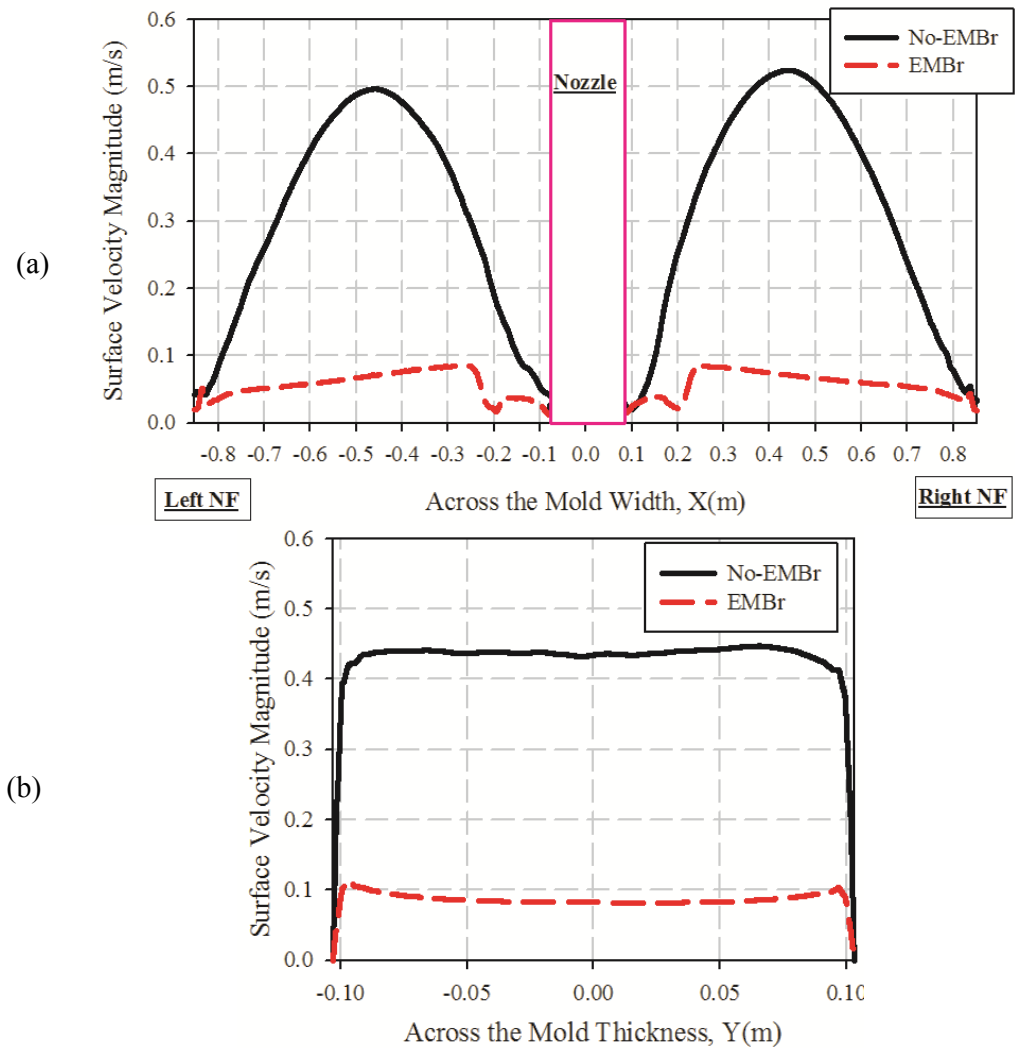


Figure 18- Variation of time-averaged velocity magnitude (a) across the width of the mold on the top surface at  $Y=0$  mm and (b) across the thickness of the mold at  $X=0.3$ m



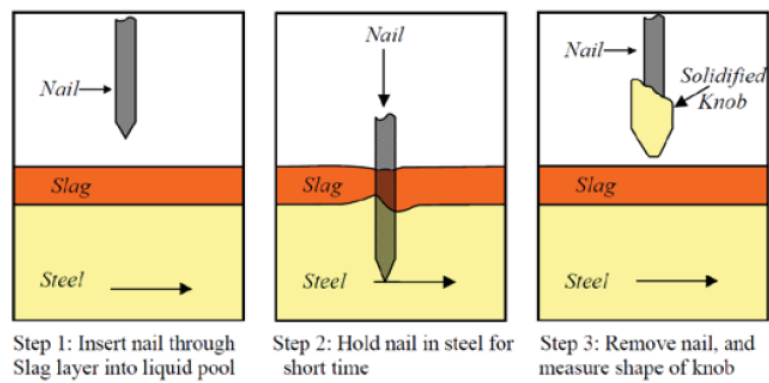


Figure 19- Nail Board Test Procedure [1]



Figure 20- Pictures of one of the nail board used for the measurements at the commercial steel caster (a) front view and (b) bottom view

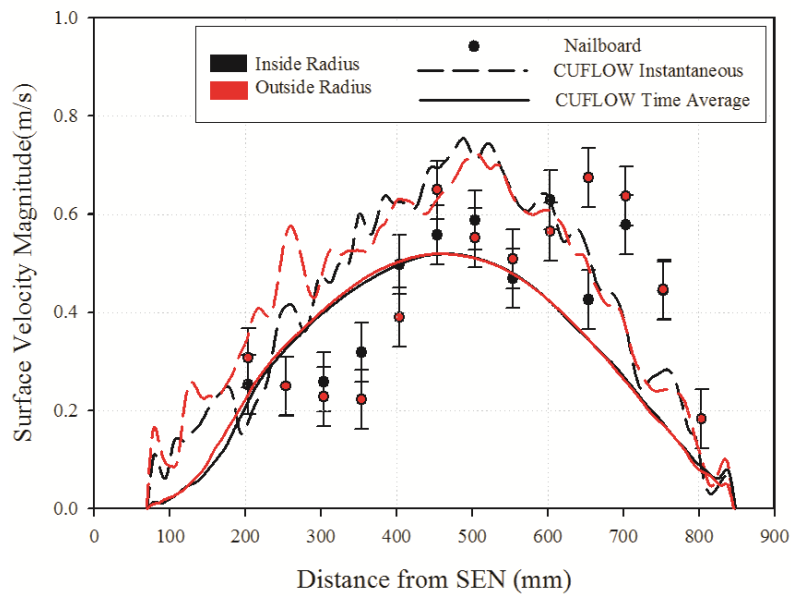


Figure 21- Comparison of measured and calculated surface velocity magnitude on the two rows of nails on the nail board

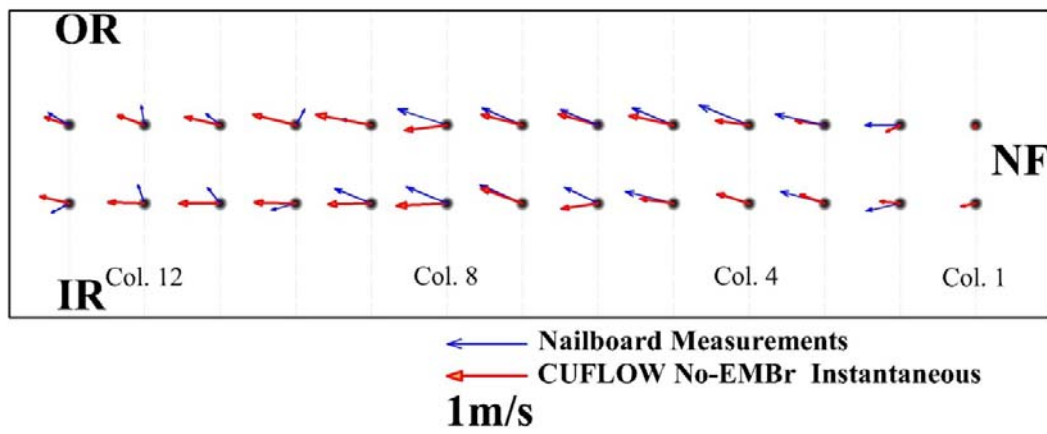


Figure 22- Comparison of measured and calculated surface velocity vectors

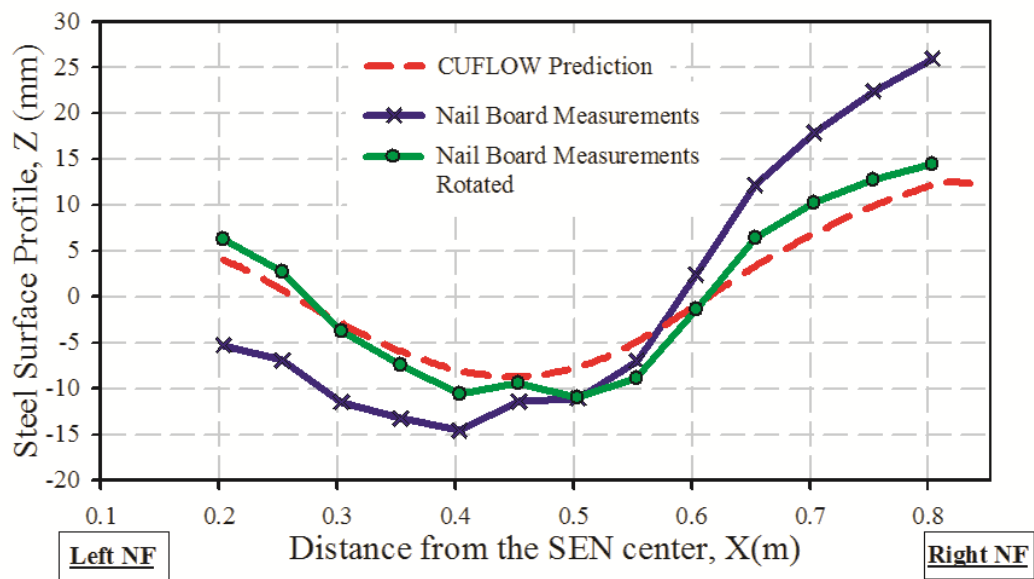


Figure 23- Comparison of measured and calculated instantaneous surface level profile  
(Rotation angle: 2.2 deg)